nanomaterials

MDPI

Article

Rationally Designed CdS-Based Ternary Heterojunctions: A Case of 1T-MoS_2 in CdS/TiO_2 Photocatalyst

Wenqian Chen [1,2,*,†], Shaomei Zhang [1,3,†], Ganyu Wang [1,3], Gang Huang [4], Zhichong Yu [1,3], Yirui Li [1,3] and Liang Tang [1,3,*]

1 Key Laboratory of Organic Compound Pollution Control Engineering, Ministry of Education, Shanghai 200444, China; shaomeizhang@shu.edu.cn (S.Z.); wgy@shu.edu.cn (G.W.); zhichongyu@shu.edu.cn (Z.Y.); yiruili@shu.edu.cn (Y.L.)
2 Shanghai Institute of Applied Radiation, Shanghai University, 20 Chengzhong Road, Shanghai 201800, China
3 School of Environmental and Chemical Engineering, Shanghai University, Shanghai 200444, China
4 Physical Science and Engineering Division King Abdullah University of Science and Technology (KAUST), Thuwal 23955-6900, Saudi Arabia; gang.huang@kaust.edu.sa
* Correspondence: wenqianchen@shu.edu.cn (W.C.); tang1liang@shu.edu.cn (L.T.)
† These authors contributed equally to this work.

Abstract: As promising heterojunction photocatalysts, the binary CdS-based heterojunctions were investigated extensively. In most of the reported CdS-based heterojunctions, however, electrons come from the semiconductor with wide band gap (e.g., TiO_2) would limit the visible-light absorption of CdS and hence lower the performance. In this work, we introduced 1T-MoS_2 to form a novel ternary heterojunction, namely CdS/1T-MoS_2/TiO_2, in which 1T-MoS_2 has more positive conduction band than CdS and TiO_2. The hydrogen evolution rate of CdS/1T-MoS_2/TiO_2 reaches 3.15 mmol g^{-1} h^{-1}, which is approximately 12 and 35 times higher than that of pure CdS and CdS/TiO_2 binary heterojunction under the same conditions, respectively. This performance enhancement could be attributed to the presence of 1T-MoS_2 and a plausible mechanism is proposed based on photoelectrochemical characterizations. Our results illustrate that the performance of CdS-based heterojunctions for solar hydrogen evolution can be greatly improved by appropriate materials selection.

Keywords: heterojunction; photocatalyst; hydrogen evolution; CdS/1T-MoS_2/TiO_2

Citation: Chen, W.; Zhang, S.; Wang, G.; Huang, G.; Yu, Z.; Li, Y.; Tang, L. Rationally Designed CdS-Based Ternary Heterojunctions: A Case of 1T-MoS_2 in CdS/TiO_2 Photocatalyst. *Nanomaterials* **2021**, *11*, 38. https://doi.org/10.3390/nano11010038

Received: 26 November 2020
Accepted: 18 December 2020
Published: 25 December 2020

1. Introduction

Semiconductor-based photocatalyst have been widely employed in the water splitting and treatment of various environmental pollutants [1]. Photocatalytic water splitting using semiconductor heterojunctions has gathered great interest recently, mostly due to efficient utilization of visible light [2]. In the past few decades, CdS-based heterojunctions have investigated extensively due to the narrow band gap of CdS (2.4 eV) [3]. Furthermore, the conduction band potential of CdS is more negative than the reduction potential of protons. Hence, CdS has a sufficient potential to reduce protons into H_2 [4,5]. The CdS-based photocatalysts have been extensively explored for the hydrogen evolution due to its suitable band gap structure and strong capacity of light absorption. However, CdS suffer from the problem of photo-corrosion wherein S^{2-} ions get easily oxidized by photogenerated holes [6]. The strategy to overcome the photo-corrosion of CdS is therefore highly desirable. Solutions including anion substitution [7,8] and the formation of a heterojunction have been proposed. In contrast to the anion substitution, combing a semiconductor with wide band gap to form heterojunctions is an alternative which is synthetically easier.

Numerous wide band gap semiconductors have been used in combination with CdS to form a Z-type heterojunction to overcome the photocorrosion of CdS by photo-generated holes h^+ [9]. Among them, TiO_2 with a band gap of ca. 3.2 eV is good choice [10]. On the one hand, both materials are cheap for practical applications. On the other hand, the CdS

with narrower band gap could use visible light more efficient. However, deeper valence band (VB) of CdS could allow the transfer of electrons from TiO_2-CB (conduction band) to CdS-VB, as illustrates in Scheme 1a. Hence, under a visible light irradiation, the binary heterojunction CdS/TiO_2 cannot effectively solve the problem of easy recombination of electrons and holes, which reduces the catalytic activity. Therefore, a third component with more positive CB to form a ternary heterojunction is a possible solution [11], as shown in Scheme 1b.

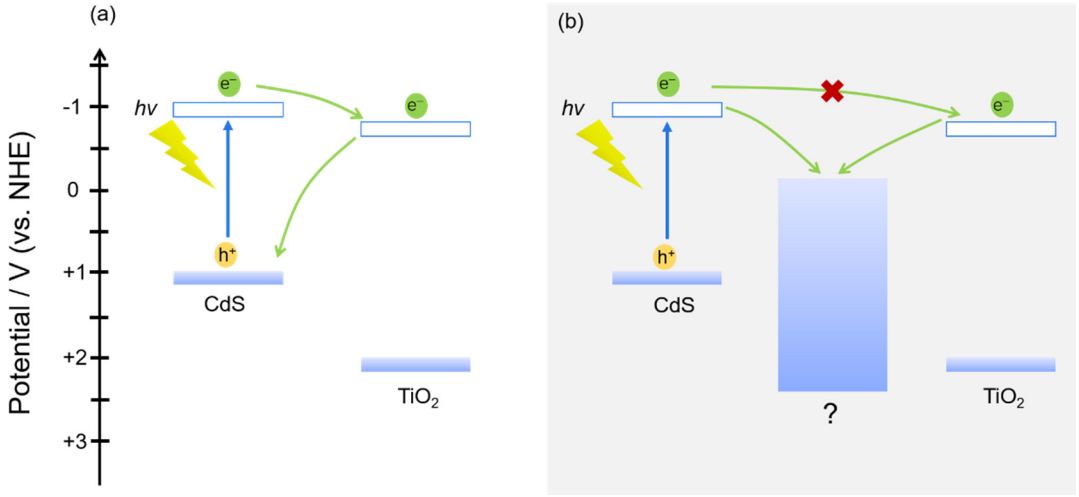

Scheme 1. (**a**) Binary CdS/TiO_2 heterojunction. (**b**) Ternary CdS-based heterojunction with a third substance that contain more positive CB.

For the third component, many compounds have been tested at several concentration ranges, such as WO_3 [11], $ZnIn_2S_4$ [12], SiO_2 [13], and Fe_3O_4 [14]. Herein, we focus on the MoS_2, which belongs to the family of layered transition metal dihalides [15–18]. MoS_2 has four morphologies: Twisted tetragonal phase (1T), hexagonal phases (1H and 2H), and rhombic phase (3R) [19]. The semiconductor phase 2H-MoS_2 is the most stable phase. 1T-MoS_2 (metal phase) can usually be obtained by chemical exfoliation of 2H-MoS_2 and embedding of various ions (Li^+, Na^+, K^+) [20]. The conductivity of 1T phase is 10^7 times higher than 2H phase [21], which facilitates the rapid flow of charge and improves the reactivity and hence were investigated widely for photocatalytic water splitting.

In this work, the CdS/1T-MoS_2/TiO_2 ternary heterojunction was synthesized by hydrothermal method. We discovered that the introduction of two-dimensional sheet-like 1T-MoS_2 can accelerate the charge transfer and increase the rate of photocatalytic hydrogen production, and the use of nanosheet 1T-MoS_2 coated around the CdS nanoparticles can prevent them from photocorrosion. Through a specific hybridization method and the energy band modification of each substance, an internal electric field is constructed to form the directional transfer of photo-generated carriers. The photocatalytic hydrogen activity reached 3.15 mmol g^{-1} h^{-1} (35 times that of binary CdS/TiO_2), indicating an important role of 1T-MoS_2 in the CdS-based heterojunctions.

2. Materials and Methods

2.1. Preparation of Photocatalysts

The CdS/TiO_2 binary heterojunction was synthesized by a hydrothermal method with anatase TiO_2 nanoparticles. TiO_2 was prepared by solvothermal method, as previously reported [22]. The $Cd(CH_3COO)_2{\cdot}2H_2O$ (AG, Adamas, 1.38 mmol) and thiourea (AG, Adamas, 5.52 mmol) were dispersed in 35 mL pure water, then the obtained TiO_2 was added, the molar ratio of TiO_2 is 15%, 25% and 35% of the Cd amount. Stir evenly and transfer to the 50 mL Teflon-lined stainless-steel autoclave. The mixture was reacted at 453 K for 5 h, followed cooled to room temperature naturally. The samples were washed

with pure water and ethanol for several times, then vacuum dried at 333 K overnight. Bare CdS was synthesized by the same method without TiO_2 [23].

The ternary CdS/1T-MoS_2/TiO_2 heterojunction was synthesized with the addition of CTAB and $(NH_4)_6Mo_7O_{24}\cdot 4H_2O$. First, CdS (0.1444 g) was added into 50 mL pure water. 10 mL of CTAB (AR, Sinopharm Chemical Reagent Co., Ltd. Shanghai, China) aqueous solution (0.01 M) was then added into above orange suspension. $(NH_4)_6Mo_7O_{24}\cdot 4H_2O$ (AG, Adamas) and thiourea (n(Mo):n(S) = 7:15, AG, Adamas) were further added to the above mixture with the Mo atoms are 25%, 35%, and 45% molar ratio of CdS. The mixture was transferred into 100 mL Teflon-lined stainless-steel autoclave, and reacted at 473 K for 24 h. The samples were centrifuged and washed with pure water and ethanol for several times, then vacuum dried at 333 K overnight. Second, the obtained binary heterojunction "CdS/1T-MoS_2-45" (45% of MoS_2) was put into 45 mL ethanol (AR, Adamas) and stirred to form suspension A, the corresponding amount of TiO_2 (the molar amount is 15%, 25%, and 35% of CdS) was then added into 15 mL ethanol and ultrasonic for 2 h to form suspension B, then suspension B was poured into suspension A. The mixture was transferred to 100 mL Teflon-lined stainless-steel autoclave, and reacted at 393 K for 2 h. The samples were obtained after washed and vacuum dried at 333 K overnight. The ternary products were named as CdS/1T-MoS_2/TiO_2-45-15, CdS/1T-MoS_2/TiO_2-45-25 and CdS/1T-MoS_2/TiO_2-45-35. The pure 1T-MoS_2 can be obtained by $(NH_4)_6Mo_7O_{24}\cdot 4H_2O$ and thiourea in accordance with the above proportion {n(Mo):n(S) = 7:15} and reaction conditions [24].

2.2. Characterization

X-ray diffraction (XRD) patterns were obtained from DX-2700 X-ray diffractometer with Cu-Kα radiation operated at 40 kV and 40 mA. Scanning electronic microscopy (SEM) images were conducted on ZEISS MERLIN Compact. Transmission electron microscopy (TEM) and high-resolution transmission electron microscopy (HRTEM) observations were performed on a JEOL JEM-2010F electron microscope operating at 200 kV. X-ray photoelectron spectroscopy (XPS) was tested on Thermo ESCALAB 250XI using Al-Kα excitation source ($h\nu$ = 1486.6 eV) and C_{1s} = 284.60 eV combined energy standard was used for charge correction. Raman spectra were detected by a Japan HORIBA system with a 532 nm laser. UV-vis diffuse reflectance spectra (DRS) were carried out on a UV-vis spectrometer (UV-2600, Shimadzu, Japan), $BaSO_4$ as whiteboard to deduct background value. The photoluminescence (PL) spectra were measured by a F-320 Fluorescence Spectrophotometer that excitation wavelength is 494 nm.

2.3. Photocatalysis

The photocatalytic reaction was conducted on an all glass automatic on-line trace gas analysis system (Labsolar-6A) and SHIMAZU gas chromatograph (GC-2014C). The hydrogen generated in the reactor was automatically entered into the gas chromatograph for detection. Fifty milligrams of catalyst was placed in the reactor and a 100 mL aqueous solution containing 10 mL of lactic acid was poured into the reactor. The reactor temperature was kept at 278 K by a low temperature thermostatic bath. The light source is a 300 W Xe lamp ($\lambda \geq 350$ nm).

2.4. Photoelectrochemical Measurements

Mott–Schottky analysis, ampere i-t curve analysis, and electrochemical impedance spectroscopy (EIS) were performed by electrochemical workstation (CHI660E instrument). The electrodes were prepared by spin-on-conductive glass process, as previously reported [25]. A three-electrode system with the electrolyte of 0.5 M Na_2SO_4 solution was used, in which the counter electrode was platinum, the reference electrode was saturated calomel electrode (SCE), and the working electrode was conductive glass coated with photocatalyst. The Mott–Schottky measurement was measured using an impedance-potential model with a voltage range of −1.5~1.5 V. The amperometric i-t curve was measured by a

300 W Xe lamp (CEL-HXF300). The EIS test was performed at a frequency range between 10^{-2} and 10^{5} Hz.

3. Results and Discussion

3.1. Structural Analysis

Figure 1 presents the XRD patterns of the binary and ternary CdS heterojunctions. XRD pattern of the bare CdS sample is consistent with the hexagonal standard CdS card (JCPDS card no. 89-2944) (Figure S1a). SEM image shown the CdS is formed by the aggregation of small nanoparticles with the particle size of ca. 100 nm (Figure S1b). Figure S1c,d shows the XRD and SEM topography of TiO_2. It can be seen that the TiO_2 is a square nanosheet of about 50 nm. Figure S2 provides the structural analysis of 1T-MoS_2 nanosheets. The 1T-MoS_2 nanosheets in this work were grown in situ on the surface of CdS nanoparticles, forming a binary heterojunction CdS/1T-MoS_2. Figure S3a shown the characteristic peak of binary heterojunction is the CdS, and there is no 1T-MoS_2 peaks were observed. This could be due to the low crystallinity of 1T-MoS_2. Moreover, the formation of CdS/1T-MoS_2 do not change the structure of CdS. A similar XRD pattern of binary CdS/TiO_2 (Figure S3b) and ternary heterojunctions were observed. Because the 2theta value of the TiO_2 (101) crystal plane and the CdS (100) crystal plane are very small, the corresponding peak of TiO_2 is not visible in Figure S3b, but it is obvious that the peak intensity around 25° is significantly enhanced. This indicates that TiO_2 and 1T-MoS_2 only interacts with the surface of CdS and does not change the crystal structure of each material. These results have confirmed the successful loading of the molybdenum disulfide and titanium dioxide on the CdS surface.

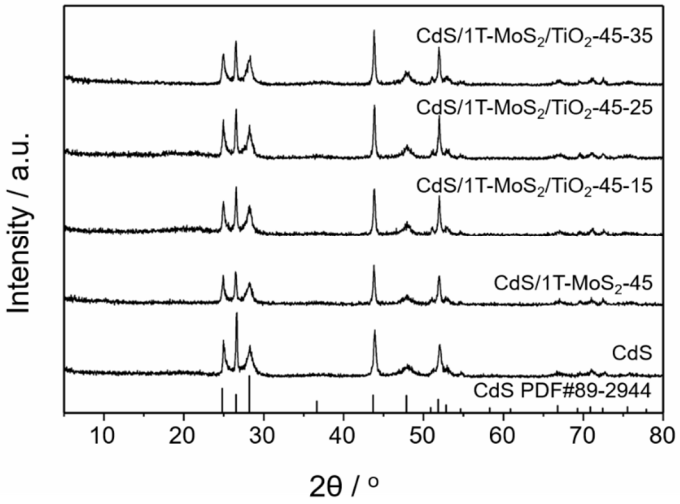

Figure 1. XRD patterns of the bare CdS, binary CdS/1T-MoS_2, and ternary CdS/1T-MoS_2/TiO_2 heterojunctions.

As shown in Figure 2a, the ternary heterojunctions are clustered together in the form of nanoparticles. At the edge of the particles, unlike pure CdS (Figure S1b), it can be clearly seen that the transparent flakes 1T-MoS_2 wrap the CdS nanoparticles, and the small square nanosheets TiO_2 are scattered and uniformly distributed on the flakes. By magnifying the edges of particles, a high-resolution transmission electron microscopy (HRTEM) is obtained. The corresponding diffraction pattern can be obtained by fast Fourier transform (FFT) at the lattice fringe of HRTEM. The distance from the diffraction spot to the center is consistent with the lattice fringe spacing on the HRTEM image. The lattice spacing calculated from FFT also matches the corresponding d value of the XRD pattern. The lattice spacing marked 2.48 Å, 9.32 Å, and 3.48 Å in the HRTEM image (Figure 2b), which respectively represent (102) crystal planes of CdS, (002) crystal planes of 1T-MoS_2, and (101) crystal planes of TiO_2. The close contact between the three substances is beneficial to the rapid transfer of photogenerated electrons, and thus facilitating the production of hydrogen. Moreover,

compared to the 2H phase, the expanded layer spacing of 1T-MoS_2 speeds up the electron flow this improves the catalytic performance of the heterojunctions. EDS element mapping (Figure 2c) shown the existence of Cd, S, Mo, Ti, O and their uniform distribution in the composites. In addition, EDS spectrum (Figure S4) provides the semi-quantitative value of each element in the sample of CdS/1T-MoS_2/TiO_2-45-15. This indicates that the main content in the heterojunction is Cd and S, while other elements exist in a small amount. This EDS result agreement well with the XRD patterns that the characteristic peaks of both binary and ternary heterojunctions are consistent with that of CdS.

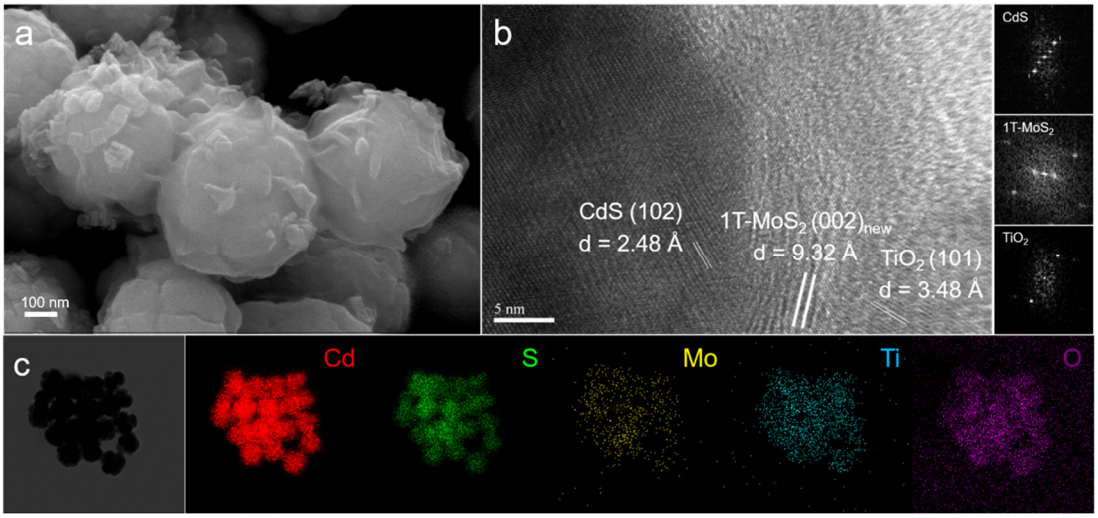

Figure 2. (**a**) SEM image and (**b**) high-resolution transmission electron microscopy (HRTEM) image of CdS/1T-MoS_2/TiO_2-45-15 heterojunction. (**c**) EDS element mapping images of Cd, S, Mo, Ti, and O in the CdS/1T-MoS_2/TiO_2-45-15.

Raman spectroscopy and X-ray photoelectron spectroscopy (XPS) were conducted for further analysis of the ternary heterojunctions, as shown in Figure 3. The characteristic peaks at 299 cm^{-1} and 597 cm^{-1} in CdS/1T-MoS_2/TiO_2-45-15 are attributed to the longitudinal optical phonon mode of CdS in the Raman spectra [26]. When CdS was coupled with 1T-MoS_2 and TiO_2, 150 cm^{-1} corresponding peaks of 1T-MoS_2 and 397 cm^{-1} corresponding peaks of TiO_2 are observed in the Raman spectrum of the composite CdS/1T-MoS_2/TiO_2-45-15 (Figure 3a), indicates the CdS has a close interaction with other two compounds. Figure S5 shown the XPS full spectrum of ternary heterojunction, which involves the composite elements of Cd, S, Mo, Ti, and O. Figure 3b shown the peaks at 404.69 eV and 411.43 eV of CdS/1T-MoS_2/TiO_2-45-15 heterojunction represent the $3d_{5/2}$ and $3d_{3/2}$ orbits of Cd^{2+}, respectively. Compared to the bare CdS (404.81 eV and 411.55 eV) [27], the low energy peaks in the heterojunctions may be due to the interaction of CdS with 1T-MoS_2 and TiO_2. Figure 3c shown the Mo peaks of 229.82 eV and 232.92 eV in the heterojunction are respectively represented by the $3d_{5/2}$ and $3d_{3/2}$ of Mo^{4+} [28]. Compared to the bare 1T-MoS_2, the peaks are shifted to the high energy, indicating the change of electronic density around Mo element. After deconvoluting the Mo 3d environment (Figure S6), the 1T phase content remains high, and an additional Mo-O bond peak appears at 233.19 eV and 235.46 eV [29,30]. As shown in Figure 3d, when the binary heterojunction CdS/1T-MoS_2-45 was coupled with TiO_2, the 2p orbital energy of Ti element is also shifted, indicates the interaction between TiO_2 and 1T-MoS_2. Therefore, Raman and XPS results further revealed the successful synthesis of CdS/1T-MoS_2/TiO_2 hetero-structured composites.

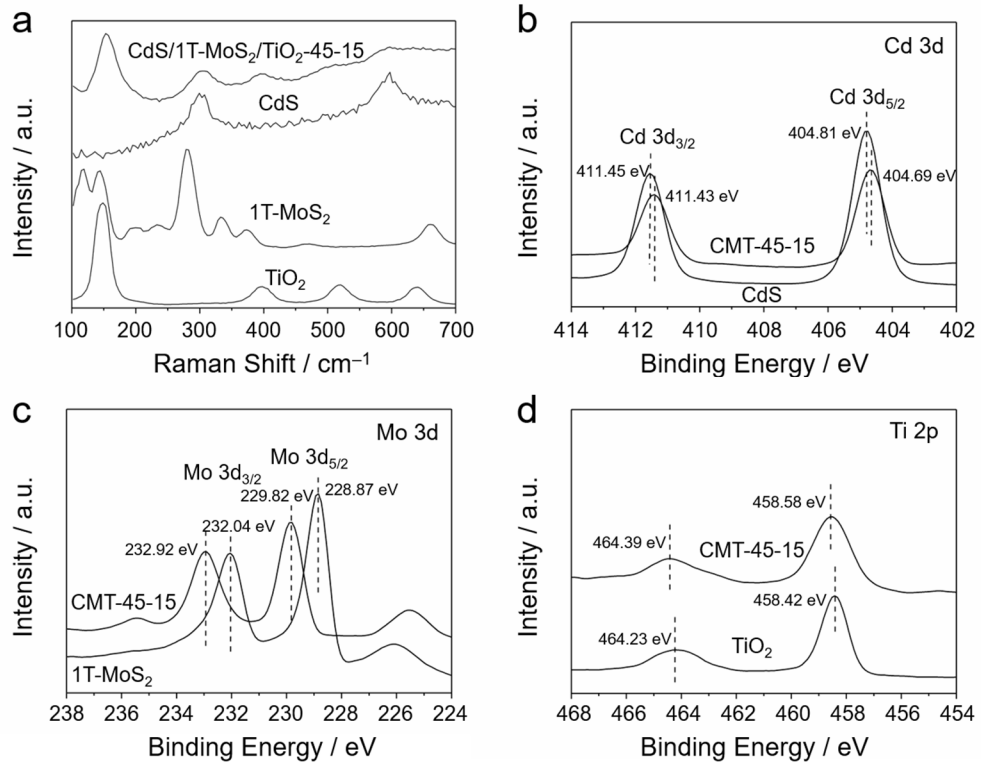

Figure 3. (**a**) Raman spectra of the bare CdS, TiO_2, and CdS/1T-MoS_2/TiO_2-45-15 samples. High resolution XPS spectra of (**b**) Cd 3d in bare CdS and CdS/1T-MoS_2/TiO_2-45-15; (**c**) Mo 3d in 1T-MoS_2 and CdS/1T-MoS_2/TiO_2-45-15; (**d**) Ti 2p in TiO_2 and CdS/1T-MoS_2/TiO_2-45-15(CMT-45-15).

3.2. Photocatalysis

The catalysts were photocatalyzed to produce hydrogen under a simulated sunlight irradiation ($\lambda \geq 350$ nm), and lactic acid was used as a reversible electron donor. Figure 4 and Figure S7 shown the hydrogen production of different materials. It can be seen from Figure S7 that the hydrogen production increases linearly with the irradiation time increased. Figure 4a shown the activity was greatly enhanced with the combined of 1T-MoS_2 in the binary CdS/TiO_2 heterojunctions. Interestingly, the activity of binary CdS/TiO_2 heterojunctions is lower than that of bare CdS, suggesting an electron transfer limitation between the wide band gap TiO_2 and CdS. Moreover, the best composition of ternary heterojunctions is CdS/1T-MoS_2/TiO_2-45-15. We will discuss the relationship between the activity and composite differences in the later section. Figure 4b provides the three times of cycle hydrogen evolution experiments on CdS/1T-MoS_2/TiO_2-45-15, indicating a stable ternary heterojunction semiconductor-based photocatalyst was obtained. Furthermore, the structure of CdS/1T-MoS_2/TiO_2-45-15 was maintained after photocatalytic reactions (Figure S8) as evidenced by XRD.

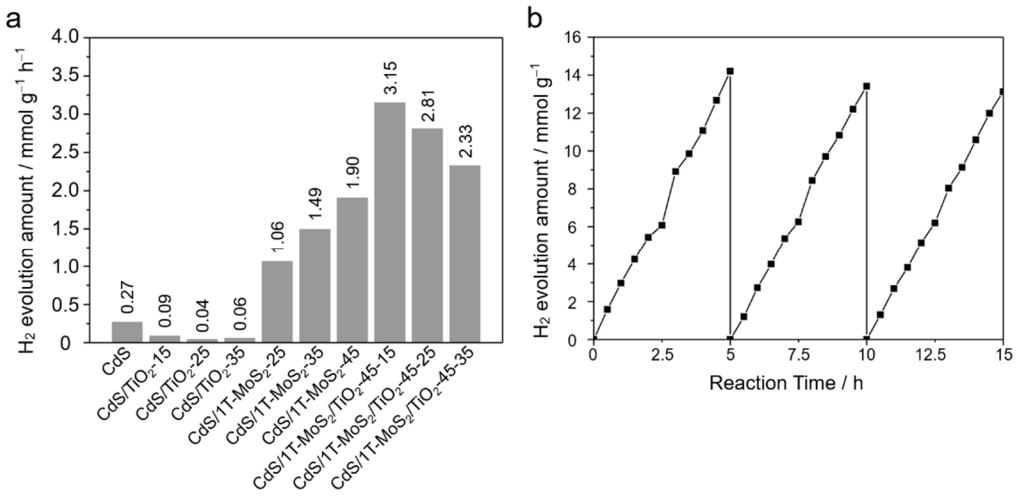

Figure 4. (**a**) Total amount of photocatalytic hydrogen production in 3 h of the bare CdS, binary, and ternary heterojunctions. (**b**) Hydrogen production cycle test of ternary CdS/1T-MoS_2/TiO_2-45-15.

3.3. Light Absorption Properties

UV-visible DRS spectra of the heterojunctions are shown in Figure 5a. The heterojunction has absorption edges at around 570 nm, which is close to the bare CdS and binary CdS/1T-MoS_2. However, different with the CdS, the visible light absorption of binary and ternary heterojunctions was enhanced in the ranges of 570–780 nm, indicates the formation of heterojunction can promote the light absorption. Figure S9a,b shown the effect of 1T-MoS_2 and TiO_2 concentrations on the light absorption of binary heterojunctions. Apparently, the absorbance increases after the addition of 1T-MoS_2, which could partly explain the hydrogen production gradually increases as its loading amount increased in heterojunctions (Figure 4a). However, the absorbance did not increase significantly when TiO_2 amounts were increased. It is due to the weak light absorption ability of white TiO_2. This suggest the addition of 1T-MoS_2 plays a key role in the enhanced light absorption properties.

3.4. Charge Carrier Dynamics

Photoluminescence (PL) spectra and photocurrent response were performed on the catalysts to further study the dynamics of photogenerated electron-hole pairs. As shown in Figure 5b, it is clear that CdS has a relatively high PL intensity. The appearance of 1T-MoS_2 will weaken the PL intensity. This result is supported by the hydrogen release amount of different samples of binary heterojunction CdS/1T-MoS_2. Afterwards, the addition of TiO_2 greatly weakened the PL intensity, indicating that the photogenerated carriers were largely captured by TiO_2, thereby inhibiting the recombination of electron-hole pairs. The EIS Nyquist plots of the catalysts were shown in Figure 5c. It is well known that the smaller the EIS spectra the lower of the charge-transfer resistance, and hence an enhanced electron transfer capability and high separation effectiveness of the photogenerated electron-hole pairs. Compared to the bare CdS and binary CdS/1T-MoS_2, the ternary CdS/1T-MoS_2/TiO_2-45-15 contain a quite small arc radius, indicates the low impedance and hence high charge separation efficiency in the ternary heterojunctions. The photocurrent response (Figure 5d) can also further illustrate the efficiency of photogenerated charge carrier separation. After repeated on-off light irradiation for several times, the response current of CdS/1T-MoS_2/TiO_2-45-15 is strong and relatively stable, which is consistent with the experimental data of PL, EIS and hydrogen evolution experiments. These results clearly indicate the presence of 1T-MoS_2 in the CdS/TiO_2 binary heterojunction promotes the electron transfer and reduces the recombination of electron hole pairs.

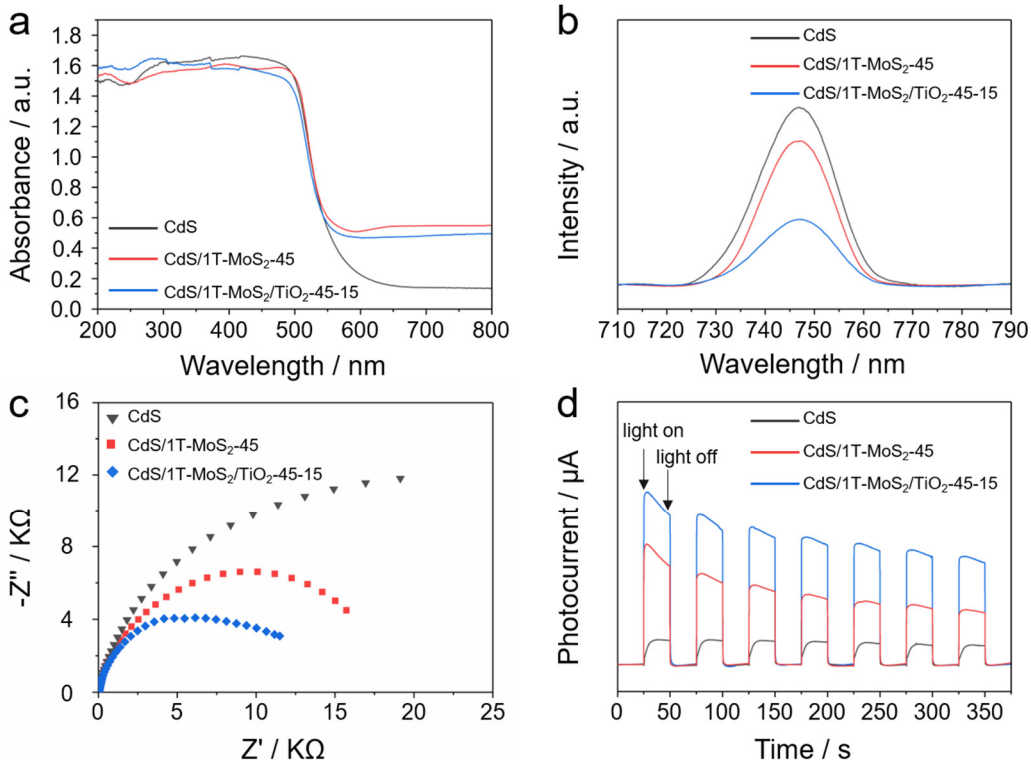

Figure 5. (**a**) UV-vis diffuse reflectance spectra (DRS), (**b**) photoluminescence (PL) spectra, (**c**) electrochemical impedance spectroscopy (EIS), and (**d**) transient photocurrent of the bare CdS, CdS/1T-MoS_2-45, and CdS/1T-MoS_2/TiO_2-45-15 samples.

3.5. Band Potential Analysis

We further analysis the band positions of three substances to explore the possible mechanism of ternary heterojunctions. Figure S10a shown the UV-vis diffuse reflection spectrum of these three single substances. Use the diffuse reflection data to obtain $(\alpha h\nu)^{1/2}$ against $h\nu$ plots and it provides the band gaps in Figure S10b, where the band gaps of CdS and TiO_2 are 2.02 eV and 2.93 eV, respectively. 1T-MoS_2 is metallic with no band gap [31]. This further confirmed by XPS in Figure S11d, which shown that the E_{VB} position of 1T-MoS_2 is ~0 V.

Furthermore, the Mott–Schottky analysis was used to determine the flat band potential (E_{FB}) of semiconductor materials. Figure S11 shows the Mott–Schottky plots of CdS, TiO_2, and 1T-MoS_2 with the frequency ranges from 300–1000 Hz. In each case, the C^{-2} values decreased as the applied potential E became more negative. This is a typical behavior for an n-type semiconductor. The E_{FB} can be estimated by extrapolating the Mott–Schottky plot linearly to the x axis intercept. The E_{CB} positions of CdS, TiO_2 and 1T-MoS_2 were estimated as -1.20 ± 0.01 V, -0.97 ± 0.02 V, and -0.43 ± 0.02 V (vs. SCE), respectively (equivalent to -0.96 V, -0.73 V and -0.19 V vs. NHE). It is known that the conduction-band minimum (E_{CBM}) is 0.1–0.3 V more negative than the E_{FB} in an n-type semiconductor [32]. Hence, the E_{CBM} values are located at ca. -1.06 V for CdS, -0.83 V for TiO_2, and -0.29 V for 1T-MoS_2 (vs. NHE). The resulting hydrogen production mechanism diagram is shown in Figure 6. It can be seen that the E_{CBM} of 1T-MoS_2 is more positive than that of TiO_2. Therefore, 1T-MoS_2 is suitable for the third substance in CdS/TiO_2 binary heterojunction. This is the origin of the high performances on ternary heterojunction.

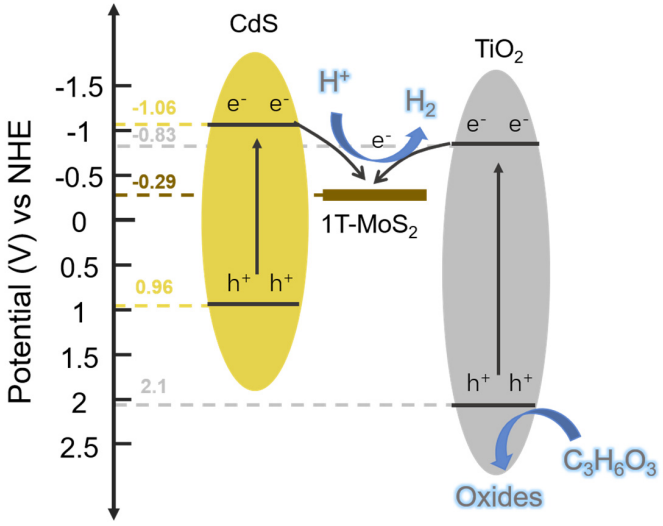

Figure 6. Schematic energy level diagram of CdS/1T-MoS_2/TiO_2 ternary system.

4. Conclusions

This study set out an efficient CdS/1T-MoS_2/TiO_2 ternary heterojunction, synthesized by a simple hydrothermal method. The presence of 1T-MoS_2 greatly promotes the photocatalytic property of binary CdS/TiO_2 heterojunctions (35 times that of binary CdS/TiO_2). This could be explained by the improvement of charge carrier dynamics (electron-hole pairs) and has been systematically discussed on the basis of PL, EIS, and photocurrent results. In addition, the metallicity and two-dimensional layered structure of 1T-MoS_2 are conducive to accelerate the electron transfer, and its coating can avoid the photo-corrosion of CdS. This greatly enhance the catalytic performance of the material and thus has great potential for CdS-based heterojunctions.

Supplementary Materials: The following are available online at https://www.mdpi.com/2079-4991/11/1/38/s1, Figure S1: (**a**) XRD pattern and (**b**) SEM image of the pure CdS nanoparticles, (**c**) XRD pattern and (**d**) SEM image of the TiO2 nanosheets, Figure S2: (**a**) XRD pattern, (**b**) TEM image, (**c**) HRTEM image, (**d**) EDS element mapping images of S, Mo, and (**e**) Raman spectra of 1T-MoS_2 nanosheets, Figure S3: XRD patterns of binary heterojunctions CdS/1T-MoS_2 (**a**) and CdS/TiO_2 (**b**), Figure S4: EDS spectrum of CdS/1T-MoS_2/TiO_2-45-15 heterojunctions, Figure S5: SEM-EDS image of CdS/ TiO_2, CdS/1T-MoS_2 and CdS/1T-MoS_2/TiO_2, EDS element mapping shows the existence of Cd, S, Mo, Ti and their uniform distribution in the composites, Figure S6: Full XPS spectrum of CdS/1T-MoS_2/TiO_2-45-15, Figure S7: Deconvolutions of Mo 3d XPS analyses of 1T-MoS_2 (**a**) and CdS/1T-MoS_2/TiO_2-45-15 (**b**) samples, Figure S8: FTIR of pure CdS, 1T-MoS_2 and CdS/1T-MoS_2/TiO_2-45-15 nanocomposites, Figure S9: (**a**) Nitrogen sorption isotherms and (**b**) corresponding pore size distribution curves of CdS and CdS/1T-MoS_2/TiO_2-45-15, Figure S10: Total amount of photocatalytic hydrogen production in 3h of (**a**) CdS/TiO_2, (**b**) CdS/1T-MoS_2, and (**c**) CdS/1T-MoS_2/TiO_2, Figure S11: XRD pattern after hydrogen production cycle of CdS/1T-MoS_2/TiO_2-45-15, Figure S12: UV-vis diffuse reflectance spectra (DRS) of (**a**) binary CdS/1T-MoS_2 and (**b**) ternary CdS/1T-MoS_2/TiO_2, Figure S13: (**a**) UV-vis diffuse reflectance spectra (DRS) and (**b**) The plot of $(\alpha h\nu)^{1/2}$ vs photo energy ($h\nu$) of CdS, 1T-MoS_2 and TiO_2, Figure S14: Mott-Schottky plots at different frequencies of (**a**) CdS, (**b**) TiO_2, and (**c**) 1T-MoS_2, (**d**) XPS-VB spectra of 1T-MoS_2.

Author Contributions: Conceptualization, W.C.; Data curation, S.Z. and G.W.; Formal analysis, S.Z.; Funding acquisition, L.T.; Investigation, W.C.; Project administration, W.C. and L.T.; Resources, L.T.; Software, Z.Y. and Y.L.; Supervision, G.H. and L.T.; Writing—Original draft, S.Z.; Writing—Review and editing, W.C. All authors have read and agreed to the published version of the manuscript.

Funding: This research was funded by National Natural Science Foundation of China (Nos. 41573096, 21707064), Program for Changjiang Scholars and Innovative Research Team in University (No. IRT_17R71), Program for Professor of Special Appointment (Eastern Scholar) at Shanghai Institutions of Higher Learning (QD2019005).

Conflicts of Interest: The authors declare no conflict of interest.

References

1. Hisatomi, T.; Kubota, J.; Domen, K. Recent advances in semiconductors for photocatalytic and photoelectrochemical water splitting. *Chem. Soc. Rev.* **2014**, *43*, 7520–7535. [CrossRef] [PubMed]
2. Sampath, S.; Sellappa, K. Ni-doped ZnO nanocrystalline material for electrocatalytic oxygen reduction reaction. *Energy Source Part A* **2019**, *42*, 719–729. [CrossRef]
3. Oladeji, I.O.; Chow, L.; Ferekides, C.S.; Viswanathan, V.; Zhao, Z. Metal/CdTe/CdS/Cd1− xZnxS/TCO/glass: A new CdTe thin film solar cell structure. *Sol. Energy Mater. Sol. Cells* **2000**, *61*, 203–211. [CrossRef]
4. Zhong, W.; Tu, W.; Feng, S.; Xu, A. Photocatalytic H_2 evolution on CdS nanoparticles by loading FeSe nanorods as co-catalyst under visible light irradiation. *J. Alloys Compd.* **2019**, *772*, 669–674. [CrossRef]
5. Chang, Y.-S.; Choi, M.; Baek, M.; Hsieh, P.-Y.; Yong, K.; Hsu, Y.-J. CdS/CdSe co-sensitized brookite H: TiO_2 nanostructures: Charge carrier dynamics and photoelectrochemical hydrogen generation. *Appl. Catal. B* **2018**, *225*, 379–385. [CrossRef]
6. Kudo, A.; Miseki, Y. Heterogeneous photocatalyst materials for water splitting. *Chem. Soc. Rev.* **2009**, *38*, 253–278. [CrossRef] [PubMed]
7. Kouser, S.; Ingampalli, S.R.L.; Chithaiah, P.; Roy, A.; Saha, S.; Waghmare, U.V.; Rao, C.N. Extraordinary changes in the electronic structure and properties of CdS and ZnS by anionic substitution: Cosubstitution of P and Cl in place of S. *Angew. Chem. Int. Ed.* **2015**, *54*, 8149–8153. [CrossRef]
8. Roy, A.; Shenoy, U.S.; Manjunath, K.; Vishnoi, P.; Waghmare, U.V.; Rao, C.N.R. Structure and Properties of $Cd_4P_2Cl_3$, an Analogue of CdS. *J. Phys. Chem. C* **2016**, *120*, 15063–15069. [CrossRef]
9. Xu, M.; Ye, T.; Dai, F.; Yang, J.; Shen, J.; He, Q.; Chen, W.; Liang, N.; Zai, J.; Qian, X. Rationally designed n–n heterojunction with highly efficient solar hydrogen evolution. *ChemSusChem* **2015**, *8*, 1218–1225. [CrossRef]
10. Sant, P.A.; Kamat, P.V. Interparticle electron transfer between size-quantized CdS and TiO_2 semiconductor nanoclusters. *Phys. Chem. Chem. Phys.* **2002**, *4*, 198–203. [CrossRef]
11. Kim, H.-I.; Kim, J.; Kim, W.; Choi, W. Enhanced Photocatalytic and Photoelectrochemical Activity in the Ternary Hybrid of $CdS/TiO_2/WO_3$ through the Cascadal Electron Transfer. *J. Phys. Chem. C* **2011**, *115*, 9797–9805. [CrossRef]
12. Mahadik, M.A.; Shinde, P.S.; Cho, M.; Jang, J.S. Fabrication of a ternary $CdS/ZnIn_2S_4/TiO_2$ heterojunction for enhancing photoelectrochemical performance: Effect of cascading electron–hole transfer. *J. Mater. Chem. A* **2015**, *3*, 23597–23606. [CrossRef]
13. Wang, J.; Sun, S.; Ding, H.; Li, W.; Wang, X. Well-Designed CdS/TiO_2/MS-SiO_2 Z-Scheme Photocatalyst for Combating Poison with Poison. *Ind. Eng. Chem. Res.* **2020**, *59*, 7659–7669. [CrossRef]
14. Bian, X.; Hong, K.; Liu, L.; Xu, M. Magnetically separable hybrid CdS-TiO_2-Fe_3O_4 nanomaterial: Enhanced photocatalystic activity under UV and visible irradiation. *Appl. Surf. Sci.* **2013**, *280*, 349–353. [CrossRef]
15. Lu, Q.; Yu, Y.; Ma, Q.; Chen, B.; Zhang, H. 2D transition-metal-dichalcogenide-nanosheet-based composites for photocatalytic and electrocatalytic hydrogen evolution reactions. *Adv. Mater.* **2016**, *28*, 1917–1933. [CrossRef] [PubMed]
16. Wu, M.-H.; Li, L.; Xue, Y.-C.; Xu, G.; Tang, L.; Liu, N.; Huang, W.-Y. Fabrication of ternary GO/g-C_3N_4/MoS_2 flower-like heterojunctions with enhanced photocatalytic activity for water remediation. *Appl. Catal. B* **2018**, *228*, 103–112. [CrossRef]
17. Chhowalla, M.; Shin, H.S.; Eda, G.; Li, L.J.; Loh, K.P.; Zhang, H. The chemistry of two-dimensional layered transition metal dichalcogenide nanosheets. *Nat. Chem.* **2013**, *5*, 263–275. [CrossRef]
18. Tang, Q.; Jiang, D.-E. Porous MS_2/MO_2 (M = W, Mo) Nanorods as Efficient Hydrogen Evolution Reaction Catalysts. *ACS Catal.* **2016**, *6*, 4953–4961. [CrossRef]
19. Lei, Z.; Zhan, J.; Tang, L.; Zhang, Y.; Wang, Y. Recent Development of Metallic (1T) Phase of Molybdenum Disulfide for Energy Conversion and Storage. *Adv. Energy Mater.* **2018**, *8*, 1703482. [CrossRef]
20. Xiong, F.; Wang, H.; Liu, X.; Sun, J.; Brongersma, M.; Pop, E.; Cui, Y. Li Intercalation in MoS_2: In Situ Observation of Its Dynamics and Tuning Optical and Electrical Properties. *Nano Lett.* **2015**, *15*, 6777–6784. [CrossRef]
21. Acerce, M.; Voiry, D.; Chhowalla, M. Metallic 1T phase MoS_2 nanosheets as supercapacitor electrode materials. *Nat. Nanotechnol.* **2015**, *10*, 313–318. [CrossRef] [PubMed]
22. Yu, X.; Kim, B.; Kim, Y.K. Highly Enhanced Photoactivity of Anatase TiO_2 Nanocrystals by Controlled Hydrogenation-Induced Surface Defects. *ACS Catal.* **2013**, *3*, 2479–2486. [CrossRef]
23. Ai, Z.; Shao, Y.; Chang, B.; Huang, B.; Wu, Y.; Hao, X. Effective orientation control of photogenerated carrier separation via rational design of a Ti_3C_2 (TiO_2)@ CdS/MoS_2 photocatalytic system. *Appl. Catal. B* **2019**, *242*, 202–208. [CrossRef]
24. Liu, Q.; Li, X.; He, Q.; Khalil, A.; Liu, D.; Xiang, T.; Wu, X.; Song, L. Gram-Scale Aqueous Synthesis of Stable Few-Layered 1T-MoS_2: Applications for Visible-Light-Driven Photocatalytic Hydrogen Evolution. *Small* **2015**, *11*, 5556–5564. [CrossRef]
25. Wu, M.; Ke, S.; Chen, W.; Zhang, S.; Zhu, M.; Zhang, Y.; Foo, M.L.; Tang, L. Optimization of the facet structure of cobalt oxide catalysts for enhanced hydrogen evolution reaction. *Catal. Sci. Technol.* **2020**, *10*, 1040–1047. [CrossRef]
26. Xu, J.; Cao, X. Characterization and mechanism of MoS_2/CdS composite photocatalyst used for hydrogen production from water splitting under visible light. *Chem. Eng. J.* **2015**, *260*, 642–648. [CrossRef]
27. Yin, X.L.; Li, L.L.; Jiang, W.J.; Zhang, Y.; Zhang, X.; Wan, L.J.; Hu, J.S. MoS_2/CdS Nanosheets-on-Nanorod Heterostructure for Highly Efficient Photocatalytic H2 Generation under Visible Light Irradiation. *ACS Appl. Mater. Interfaces* **2016**, *8*, 15258–15266. [CrossRef]

28. Li, Z.; Sun, P.; Zhan, X.; Zheng, Q.; Feng, T.; Braun, P.V.; Qi, S. Metallic 1T phase MoS_2/MnO composites with improved cyclability for lithium-ion battery anodes. *J. Alloys Compd.* **2019**, *796*, 25–32. [CrossRef]
29. Chen, X.; Wang, Z.; Wei, Y.; Zhang, X.; Zhang, Q.; Gu, L.; Zhang, L.; Yang, N.; Yu, R. High Phase-Purity 1T-MoS_2 Ultrathin Nanosheets by a Spatially Confined Template. *Angew. Chem. Int. Ed.* **2019**, *58*, 17621–17624. [CrossRef]
30. Pi, Y.; Li, Z.; Xu, D.; Liu, J.; Li, Y.; Zhang, F.; Zhang, G.; Peng, W.; Fan, X. High Yield Exfoliation of WS2 Crystals into 1–2 Layer Semiconducting Nanosheets and Efficient Photocatalytic Hydrogen Evolution from WS_2/CdS Nanorod Composites. *ACS Sustain. Chem. Eng.* **2017**, *5*, 5175–5182. [CrossRef]
31. Dong, N.; Li, Y.; Zhang, S.; Zhang, X.; Wang, J. Optically Induced Transparency and Extinction in Dispersed MoS_2, $MoSe_2$, and Graphene Nanosheets. *Adv. Opt. Mater.* **2017**, *5*, 1700543. [CrossRef]
32. Matsumoto, Y. Energy positions of oxide semiconductors and photocatalysis with iron complex oxides. *J. Solid State Chem.* **1996**, *126*, 227–234. [CrossRef]